

## Field characterization of wave-induced underwater light field fluctuations

Pierre Gernez<sup>1,2</sup> and David Antoine<sup>2</sup>

Received 30 July 2008; revised 6 March 2009; accepted 24 April 2009; published 27 June 2009.

[1] A field characterization of the amplitude and periods of the underwater light field fluctuations is presented on the basis of field measurements of the downward and upward irradiances at a deep-sea mooring in the Mediterranean Sea (BOUSSOLE site). The optical time series at this site includes multispectral irradiance measurements at two depths and irradiance profiles taken from free-fall radiometers. It is already several years long and is paralleled by a time series of wind and waves. When pooled together, both data sets provide an opportunity to complement previous field experiments dedicated to the understanding of underwater light fluctuations, which were mostly carried out in coastal waters and essentially for the downward irradiance, by exploring more systematically the electromagnetic spectrum and the range of environmental parameters. In addition, the characteristics of the upward flux are also investigated. The behavior of the amplitude and period of the  $E_d$  fluctuations are coherent with previous findings, although a more global picture is provided. The conditions for maximum fluctuations under clear skies are for wave heights of  $\sim 0.5$  m or wind speeds between  $\sim 1$  and  $5$  m s<sup>-1</sup>. Fluctuations are reduced under clear skies for wave heights  $> \sim 1.5$  m or for wind speeds  $> 7$  m s<sup>-1</sup>. The dominant periods of the fluctuations in the upward flux are changing in parallel to those in the downward flux. The amplitude of the fluctuations in the upward flux is, however, evolving in the opposite direction as compared to the downward flux, e.g., decreasing when the water becomes clearer.

**Citation:** Gernez, P., and D. Antoine (2009), Field characterization of wave-induced underwater light field fluctuations, *J. Geophys. Res.*, 114, C06025, doi:10.1029/2008JC005059.

### 1. Introduction

[2] Within the upper ( $\sim 0$ – $100$  m) lit layers of the ocean, the intensity and spectral composition of the underwater light field vary considerably, in particular when expressed in terms of the planar downward irradiance,  $E_d$ , with

$$E_d = \int_{\phi=0}^{2\pi} \int_{\theta=0}^{\pi/2} L(\theta, \phi) \cos(\theta) d\theta d\phi, \quad (1)$$

where  $L(\theta, \phi)$  is the radiance for zenith angle  $\theta$  and azimuth  $\phi$ .

[3] Under a perfectly flat air-water interface and constant above-surface irradiance,  $E_s$ , and assuming horizontally homogeneous in-water inherent optical properties, the only changes in  $E_d$  at a given wavelength  $\lambda$  would be along the

vertical, as depicted by the diffuse attenuation coefficient for the downward irradiance,  $K_d$ , with

$$K_d = -d[\ln(E_d(z))]/dz. \quad (2)$$

[4] Although the assumption of horizontally homogeneous ocean optical properties is possibly invalid in some specific situations or for large horizontal scales, it is considered valid here. Therefore the assumption is made that horizontal gradients in irradiance, if any, and again assuming a stable  $E_s$ , originate solely from refraction of solar irradiance across a rough air-water interface, which is actually the general situation in the oceanic environment.

[5] This phenomenon is well known and usually referred to as the *wave focusing* of underwater radiance or irradiance, or *fluctuations* of the underwater light field. The principal goal of this article is to present an extensive field characterization of these fluctuations as a function of the air-water interface characteristics, themselves indirectly depicted through environmental parameters (e.g., wind speed). The view point is that of a series of sensors positioned at fixed depths with respect to ground and collecting data during several of the typical timescales of the fluctuations. It is, therefore, a study of the temporal characteristics of these fluctuations. Stability of the above-water irradiance during the measurement sequence is a

<sup>1</sup>ACRI-st, Sophia Antipolis, France.

<sup>2</sup>UMR 7093, Laboratoire d'Océanographie de Villefranche, CNRS-UPMC Paris 06, Villefranche-sur-mer, France.

necessary condition, so that intermittent and possibly fast transitions between clear sky and clouds are not considered. Irradiance changes of longer timescales, i.e., diurnal to seasonal, are not considered as well.

[6] Improving the knowledge of the characteristics of these fluctuations is of interest to a number of scientific domains. Underwater imaging or imaging of underwater objects from above the sea surface is presently a focus area that necessitates major improvements in the field characterization of the fluctuations and their modeling [e.g., *Schippnick*, 1988]. Arrays of radiometers deployed at appropriate depths might be used to map wave heights and periods from the statistical analysis of irradiance fluctuations. This possibility has already been suggested several decades ago [*Schenck*, 1957], yet never applied, at least to our knowledge. In the field of biological oceanography, studies about animal vision require the knowledge of the amplitude and period of the fluctuations [e.g., *McFarland and Loew*, 1983]. The response of phytoplankton to these fluctuations remains also an open question. A series of experiments in the 1980s supports the hypothesis of photosynthetic adaptation of microalgae to high-frequency light fluctuations [*Frechette and Legendre*, 1978; *Legendre et al.*, 1986; *Queguiner and Legendre*, 1986; *Walsh and Legendre*, 1983], whereas a later study does not show any influence on the photosynthetic response for a particular marine chlorophyte, *Dunaliella tertiolecta* [*Stramski et al.*, 1993]. Finally, and from a practical viewpoint, a better characterization of these fluctuations might indicate how data collection and processing protocols can be improved for radiometric data collected at sea, for instance from free-falling radiometers [e.g., *Zibordi et al.*, 2004].

[7] Numerous theoretical studies were undertaken with the aim of parameterizing the time and space scales of  $E_d$  fluctuations as a function of the air-water interface characteristics. A review of such studies, in particular the body of work performed in Poland and Russia in the 1970s, is provided in the study by *Walker* [1994]. More recently, *Zaneveld et al.* [2001] analyzed the problem in terms of the deviation from the plane-parallel assumption that the fluctuations imply, and the practical implication when deriving  $K_d$  near the surface. The variety and complexity of the physical mechanisms make simplifying assumptions unavoidable in such theoretical approaches (e.g., ignoring scattering by particles or bubbles; simplifying the wave-shape). Field measurements are, therefore, essential for validation of the theoretical findings, and many studies based on field measurements were also conducted as early as in the 1960s [e.g., *Dera and Gordon*, 1968]. They were often performed at a single wavelength in the green part of the electromagnetic spectrum, which was imposed by the technology used at that time for the filters, and which also corresponded to the maximum of transparency for the coastal waters under scrutiny [e.g., *Dera and Gordon*, 1968; *Snyder and Dera*, 1970; *Stramski*, 1986; *Dera et al.*, 1993]. More recently, the spectral behavior of the fluctuations in the visible range was analyzed in the clear waters of the Sargasso Sea [*Stramska and Dickey*, 1998]. Because of the punctual nature of these experiments, they didn't explore a large range of environmental properties, in terms of wind speed, wave height and period, diffuseness of the incoming irradiance, and finally, water transparency

("...more and better data are needed..."), as pointed out by *Stramski* [1986].

[8] Although much is already known from these works about the period and amplitude of the irradiance fluctuations, building a synthesis is difficult from the variety of experiments already performed (different wavelengths, measurement depths, environment conditions). Some of the main facts can be listed below. The fluctuations of  $E_d$  are created by the focusing of sunlight rays refracted by surface gravity and capillary waves [*Dera and Gordon*, 1968; *Schenck*, 1957; *Snyder and Dera*, 1970]. They are maximal under clear skies and within the first ten meters [*Dera*, 1970], although sometimes observed down to 35 m in clear waters [*Stramska and Dickey*, 1998]. The focusing depth depends on the steepness of the waves [*Schenck*, 1957]. The spectral density of the focusing fluctuations exhibits much higher frequency contents than the surface wave spectral density [*Walker*, 1994]. The characteristics of the fluctuations depend on the environmental conditions, with focusing occurring favorably for moderate winds (between about 2 and 5 m s<sup>-1</sup>), when the surface irradiance diffuseness is less than 40% and when the sun zenith angle is less than 40° [*Stramski*, 1986]. The fluctuations are not regular and are characterized by very bright flashes of about 20 ms [*Stramski*, 1986]. Under a totally overcast sky, focusing due to capillary waves is minimal; some fluctuations nevertheless exist as a result of the attenuation over the fluctuating path length created by swell. In this case, the irradiance fluctuations are correlated with the water surface displacement due to wave motion [*Stramska and Dickey*, 1998].

[9] The goal of this article is to extend the characterization of underwater light fluctuations based on a data set of field measurements of the downward and upward irradiances taken from a mooring at a deep (>2400 m) ocean site in the north western Mediterranean Sea (BOUSSOLE site [*Antoine et al.*, 2006]). The optical time series at this site includes multispectral irradiance measurements at 2 fixed depths as well as irradiance profiles taken from free-fall radiometers. It is now several years long, and is paralleled by a time series of environmental parameters (including wind and waves) at the same location. When pooled together, both data sets provide an opportunity to complement previous field experiments, which were mostly carried out in coastal waters and essentially for the downward irradiance, by exploring more systematically the electromagnetic spectrum and the range of environmental parameters, such as wave heights and periods, water clarity and diffuseness of the incoming irradiance. In addition, the characteristics of the upward flux are also investigated.

[10] This work is not only feasible thanks to the length of the time series, but also thanks to the design of the measurement platform that makes it extremely stable and insensitive to wave motions [*Antoine et al.*, 2008a], which allows reliable  $E_d$  measurements to be performed close to the surface, where fluctuations are maximal.

## 2. Data and Methods

### 2.1. Measurement Site

[11] The BOUSSOLE site is located in the Ligurian Sea, one of the basins of the North Western Mediterranean Sea,

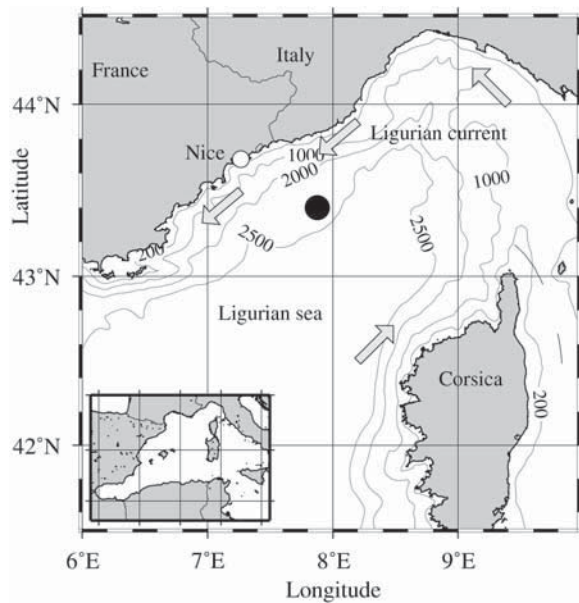


**Figure 1.** The area of North Western Mediterranean Sea where the BOUSSOLE mooring is deployed (solid circle).

at 60 km offshore from the coast (see Figure 1). Water depth at this site is 2440 m, and waters are permanently of the Case 1 type [Antoine *et al.*, 2008b], following the definition of Morel and Prieur [1977]. The annual average of the cloud cover is as low as 50% (based on the *International Satellite Cloud Climatology Project* (ISCCP) data [Rossow and Schiffer, 1991]), which ensures a high density of cloud-free observations. Ocean currents are usually weak ( $<20 \text{ cm s}^{-1}$ ), because the selected position is in the central area of the cyclonic circulation that characterizes the Ligurian Sea [Millot, 1999], which is important for the stability of the measurement platform. The dominant winds are from the west to southwest and northeast sectors.

[12] A thorough description of the range of environmental properties relevant to the problem of irradiance fluctu-

ations at the BOUSSOLE site will be provided later on (section 3.3).

## 2.2. Measurement Platform and Instrumentation

[13] The measurement platform is the BOUSSOLE buoy [Antoine *et al.*, 2008a], which was specifically designed to routinely measure radiometric quantities in the oceanic environment. The buoy is a 25-m-long tubular superstructure fixed on a 1.8-m-diameter buoyancy sphere, anchored on the seafloor via a single Kevlar cable. The sphere is at a depth of 17 m, out of the effect of most surface waves for this site. The action of Archimedes thrust and anchoring, combined to the low drag of this so-called “transparent-to-swell” superstructure, ensures the stability of the platform (no heave and low tilt). Radiometers are placed at the end of two horizontal arms in order to avoid shading by the platform (schematic drawing in Figure 2). The nominal depths of the upper and lower arms ( $z_u$  and  $z_l$  respectively) are those depths measured when the buoy is at equilibrium and the sea surface is flat. They were slightly different during successive deployments:  $z_u$  is between 2.7 m and 3.7;  $z_l$  is between 8 m and 8.7 m. The water height above the radiometers varies when swells come through. The important point here is that the radiometers can be considered fixed with respect to ground and, therefore, to the mean sea level. Therefore, from now on, and for the sake of simplicity, measurements will be referred to measurements at the two nominal depths, i.e.,  $z_u$  and  $z_l$ .

[14] The above-water irradiance,  $E_s$ , and the in-water downward and upward irradiances are measured with a set of Satlantic OCI-200 radiometers, which are calibrated in the manufacturer’s premises about every six months. These cylindrical instruments have an 8.9-cm (3.5 in) diameter, with seven cosine collectors on their upper face plate, each of 8 mm diameter and collecting data in seven 10-nm-wide spectral bands (412, 442, 490, 510, 560, 665 and 683 nm). Adequate measures have to be taken to minimize or eliminate biofouling, which is consubstantial with moored instruments. Instruments are cleaned by divers every two

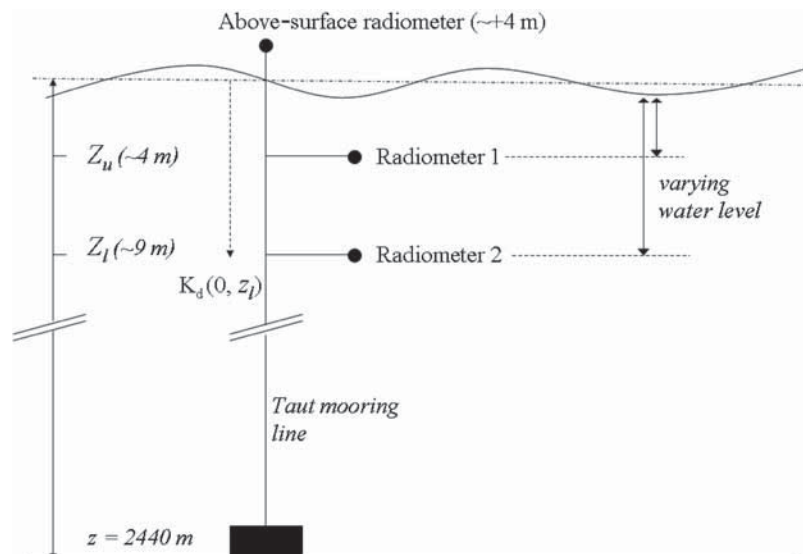


**Figure 2.** Schematic illustration of the installation of radiometers on the BOUSSOLE mooring.

weeks, in addition to the use of copper shutters, rings and tape (on the instrument bodies), so that biofouling is maintained at a very low level. This is achievable because biofouling is much less severe in the clear offshore waters at BOUSSOLE than it can be, for instance, in turbid coastal environments. Possible contamination that would have developed in spite of these procedures is identified by comparison of the data collected before and after the cleaning operations, which allows either elimination or correction of the corrupted data. The way the correction is performed is not further discussed because the corresponding data are not used here.

[15] The acquisition frequency is 6 Hz, so that about 360 measurements are collected during each of the acquisition sequences that last 1 minute. The Nyquist frequency, i.e., the highest frequency possibly analyzed, is, therefore, of 3 Hz, which allows investigation of timescales longer than 0.34 seconds. Extremely short bright flashes ( $< \sim 20$  ms), which occurs near the surface [Stramski, 1986], cannot be resolved with this sampling frequency. The data collection scenario includes a 1-minute acquisition sequence every 15 minutes from dawn to dusk.

[16] The atmospheric pressure, wave height, wave period and wind speed are collected every hour by a meteorological buoy deployed nearby the BOUSSOLE site by Météo-France.

[17] Multispectral upward and downward irradiances profiles have been also performed during monthly cruises at the BOUSSOLE site [Antoine *et al.*, 2006], using a free falling SeaWiFs Profiling Multichannel Radiometer (SPMR; 6Hz acquisition frequency). A total of 586 profiles were collected in parallel to the buoy deployments analyzed here.

### 2.3. Data Processing

[18] Two sister buoys have been rotated about every six months for maintenance since 6 September 2003. At the time this article is written  $\sim 47\,000$  sequences of acquisition had been collected at each measurement depth during daylight. A series of tests must be performed in order to eliminate measurement sequences during which undesirable changes of environment occurred, which would prevent a meaningful analysis of the irradiance variations related to interface changes.

[19] A first test verifies that the above-surface irradiance was stable during the measurement sequence, by checking that its coefficient of variation, i.e., the standard deviation to mean ratio, is lower than 5%. The second test eliminates measurements that were taken with the buoy being excessively tilted (tilt  $> 10^\circ$ ). Oscillations of about  $\pm 1$  degree occur around the average buoy tilt, which have a negligible impact on  $E_d$ . The third test verifies that the buoy was within 1 m of its nominal water level, i.e., the lower arm being not deeper than 10 m. After these tests were applied, 13300 reliable  $E_d$  series were kept for each measurement depth.

[20] The analysis of the irradiance variations will be expressed (indexed) as a function of several parameters, some of which are directly taken from the data set, i.e., wavelength, wave height and wind speed, whereas others are computed as described below.

[21] The sun zenith angle,  $\theta_s$ , is computed from the geographical coordinates of the site and the time of the

day. The minimum is  $21^\circ$  at solar noon for the summer solstice, and the maximum is simply determined by the limit above which underwater measurements become impracticable, i.e.,  $\sim 85^\circ$ .

[22] The ratio between the actual  $E_s$  at 442 nm and its theoretical clear-sky value is computed. It will be referred to as  $r_{es}$ , and will be used to describe the average reduction of the above-surface irradiance by clouds. The theoretical value is computed from Gregg and Carder [1990], using the atmospheric pressure given by the meteorological buoy, an average relative humidity of 80%, the ozone content provided by the TOMS satellite product, and a maritime aerosol model from Shettle and Fenn [1979] with an optical thickness of 0.2 at 550 nm. Values of  $r_{es}$  over 1 are theoretically unrealistic for a truly clear sky; they may occur when the sky is clearer than assumed from the above parameters or when scattered clouds in the periphery act to reflect greater irradiance amounts to the sensor.

[23] A diffuse attenuation coefficient for the downward irradiance,  $K_d$ , is determined as:

$$K_d = - \frac{\ln[E_d(z_1) / E_d(0^-)]}{z_1}, \quad (3)$$

where  $E_d(z_1)$  is the lower arm  $E_d$  measurement and  $E_d(0^-)$  is the downward irradiance just below the sea surface. It is simply  $E_s$  reduced by transmission across the air-water interface, i.e.,  $E_s$  times 0.97 [Austin, 1974].  $K_d$  is given at 490 nm. The irradiance reflectance,  $R$ , is also determined:

$$R = \frac{E_u(0^-)}{E_d(0^-)}, \quad (4)$$

where  $E_d(0^-)$  is computed as described above for the computation of  $K_d$ , and  $E_u(0^-)$  is the upward irradiance just beneath the surface, which is obtained from:

$$E_u(0^-) = E_u(z_1) e^{K_u z_1}, \quad (5)$$

where  $K_u$  is the diffuse attenuation coefficient for the upward irradiance, itself computed from the measurements of  $E_u$  collected at the two depths:

$$K_u = - \frac{\ln[E_u(z_1) / E_u(z_u)]}{\Delta z}, \quad (6)$$

Both  $K_d$  and  $R$  are combined to retrieve the total absorption and backscattering coefficients,  $a$  and  $b_b$ , following the inversion scheme proposed by [Morel *et al.*, 2006].

[24] Two parameters are used to characterize the irradiance fluctuations: the amplitude and the frequency content. Both were determined for each of the 13300 valid series of 360  $E_d$  acquisitions. The amplitude is quantified by the coefficient of variation, CV, computed as:

$$CV = 100 \frac{\sigma_M}{\mu}, \quad (7)$$

where  $\mu$  is the median and  $\sigma_M$  is the standard deviation relative to the median within the 360 measurements.

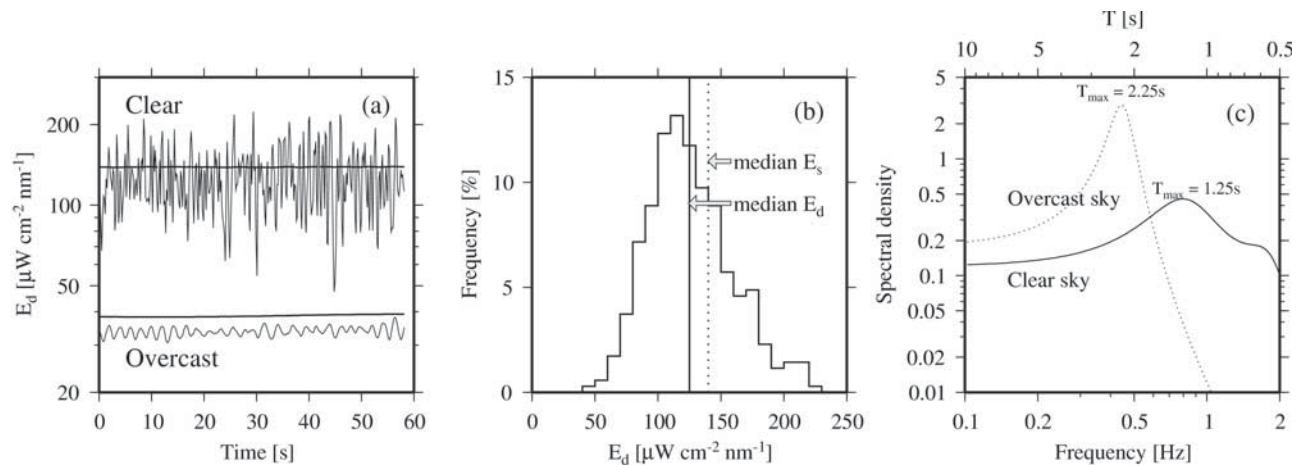


**Figure 3.** (a) Measurement sequences for  $E_d(z_u)$  at 510 nm, performed on 1 August 2007 under a clear sky (upper curve) and on 21 August 2007 under an overcast sky (lower curve), both at 1200 UTC. The values of  $E_s(510)$  are superimposed (thick lines). (b) Histogram of  $E_d(z_u)$  at 510 nm corresponding to the clear-sky data shown in Figure 3a (the histogram for the overcast sky measurement is not shown because it is a single bar). (c) Spectral densities (see text) of  $E_d(z_u)$  for the clear-sky and overcast-sky measurement sequences displayed in Figure 3a, as indicated.

[25] The frequency content of the fluctuations is characterized by their spectral density, which is also called the Variance spectrum. This spectral density is computed by means of an autoregressive model, whose details are provided in appendix.

### 3. Results

#### 3.1. Hierarchical Presentation of the Results

[26] Because the parameters that either generate irradiance fluctuations (interface roughness) or modify their properties ( $\theta_s$ ,  $K_d$ ,  $\lambda$ , ...) may vary during a measurement sequence and from one measurement sequence to another one, some organization of the results is needed. Therefore the presentations in the first four subsections below are restricted to the irradiance fluctuations at 510 nm and as measured at  $z_u$ . The choice of this wavelength is to allow comparison with previous studies (mostly performed around 500–520 nm), and the selection of the upper measurement depth is because fluctuations are a priori maximal close to the surface. For this depth and wavelength, two typical examples of measurement and data processing are first presented, and then the full data set is explored. Clear and overcast skies are separately examined. The depth and spectral changes of the fluctuations are subsequently analyzed. Finally, results are presented for the fluctuations of the upward irradiance.

#### 3.2. Examples of Measurement and Data Processing

[27] Two examples of  $E_d(z_u, 510)$  measurements are shown in Figure 3a. One is a typical example of wave focusing under a clear sky (measurements taken on 1 August 2007 at 1200), with a sun zenith angle of 26 degrees, a wind speed of  $5.6 \text{ m s}^{-1}$ , a wave height of 0.5 m and a wave period of 4s. Under these conditions,  $E_d$  shows intense ( $\text{CV} \sim 27\%$ ) and fast ( $T_{\max} \sim 1.2\text{s}$ ) variations. The fluctuations are intense enough for  $E_d(z_u)$  to repeatedly exceed the above water irradiance. The distribution of the fluctuations is asymmetric with respect to the median

(Figure 3b). The spectral density has a maximal content around 0.8Hz, which corresponds to a period of 1.25 seconds (Figure 3c).

[28] The second example is typical of fluctuations under an overcast sky (measurements taken on 21 August 2007 at 1200), with a sun zenith angle of 31 degrees, a wind speed of  $6.2 \text{ m s}^{-1}$ , a wave height of 0.7 m and a wave period of 5s. Under these conditions,  $E_d$  is much more stable than for the clear sky measurements, and remains lower than  $E_s$  (Figure 3a). The coefficient of variation is 4% and the spectral density is maximal around 0.44 Hz, i.e., a period of 2.25 seconds (Figure 3c).

[29] All intermediate situations are possible between these two somewhat extreme cases, depending on illumination conditions, interface characteristics and water clarity. Therefore the range of environmental conditions is now assessed, and the fluctuations are subsequently analyzed as a function of the various parameters describing the environment.

#### 3.3. Environmental Parameters and Data Classification

[30] For a given state of the air-sea interface, the first determinant of the irradiance fluctuations is the diffuseness of the incoming radiation. In the overall data set,  $r_{es}$  varies from 0.1 to 1.2 (Figure 4a), with more than 70% of the values above 0.9, and only 19% lower than 0.6.

[31] As far as the air-sea interface is concerned, the significant wave height, depicted here by the  $H_{1/3}$  parameter (average of the wave height within the upper third of the wave height distribution), varies from 0 to 3 m (Figure 4b, thick line), which means that the wave height may get up to  $\sim 6$  m. Nevertheless, a large proportion of the waves have  $H_{1/3} < 1$  m. The typical wave period is between 3 and 6s (Figure 4b, thin line), with episodic longer waves ( $T \sim 10$  seconds). Wind speeds less than  $5 \text{ m s}^{-1}$  dominate (Figure 4c), with, however, stronger winds up to  $\sim 15 \text{ m s}^{-1}$ .

[32] The  $K_d$  distribution (Figure 4d) is skewed toward low values, with most values between 0.03 and  $0.1 \text{ m}^{-1}$ , and a maximum of values around  $0.05 \text{ m}^{-1}$ . This is typical of

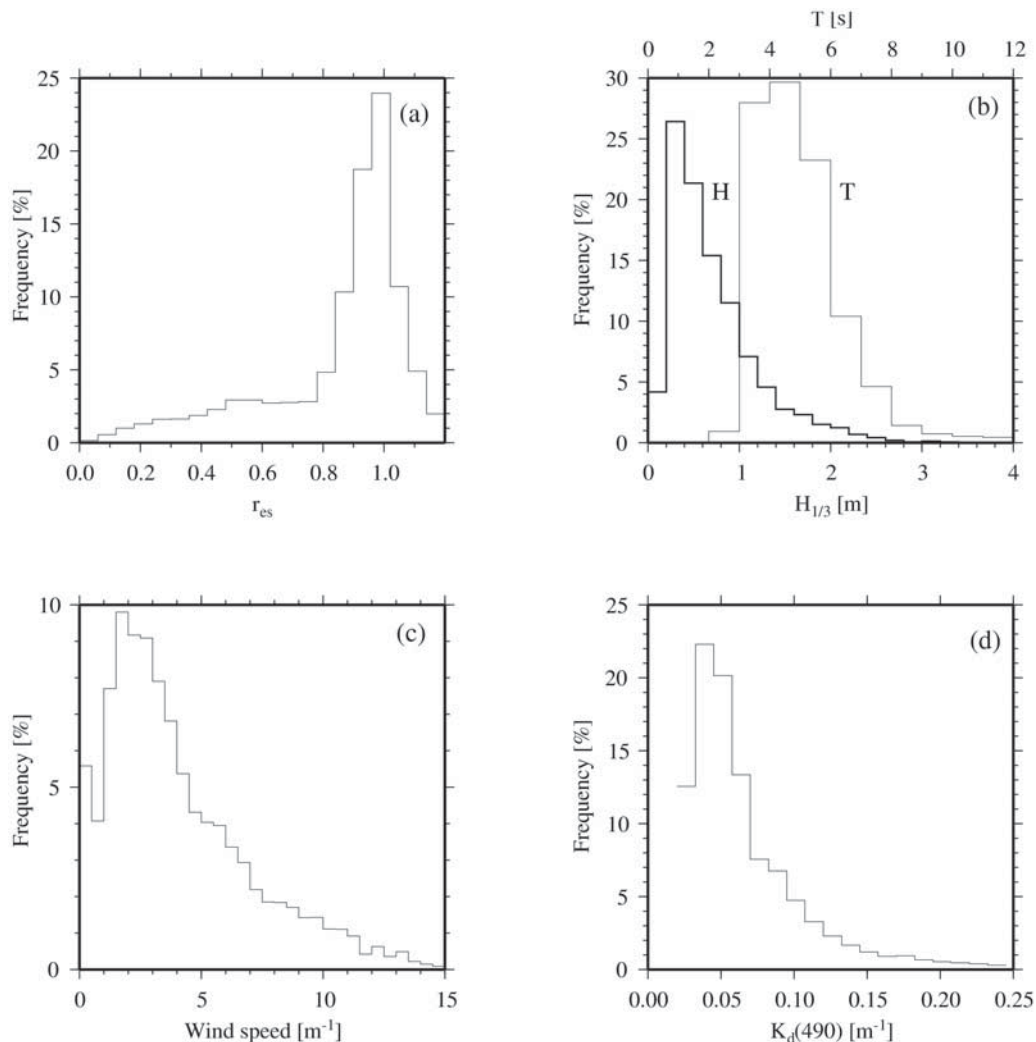


**Figure 4.** Histograms of (a)  $r_{es}$ , (b) wave height ( $H$ ; thick line, bottom axis) and wave period ( $T$ ; thin line, top axis), (c) wind speed, and (d)  $K_d(490)$ . These histograms are built from data recorded at the BOUSSOLE site from September 2003 to December 2006.

clear, oligotrophic, waters. During the spring phytoplankton bloom, greater values are recorded, up to  $0.25 \text{ m}^{-1}$ . They would correspond to chlorophyll concentrations  $\sim 3\text{--}5 \text{ mg m}^{-3}$  according to *Morel and Maritorena* [2001].

[33] In order to organize the analysis, the data set has been first split into a clear-sky and an overcast-sky subsets. The separation is based on the distribution of CV as a function of  $r_{es}$ , which clearly shows two regimes (Figure 5). On Figure 5, the gray symbols are all individual measurements, and the solid symbols are average values computed for 12 equidistant  $r_{es}$  classes. When  $r_{es} < 0.6$  (overcast skies), CV is low, 3% on average, and independent of  $r_{es}$ . When  $r_{es} > 0.85$ , CV is large (20% on average) and varies a lot. The first subset, which will be referred to as the *CLOUD* data set, includes  $\sim 2500$  cases. The change of  $r_{es}$  within this data set is essentially due to the change of the cloud optical thickness for homogeneous cloud covers. The second subset, which will be referred to as the *SUN* data set (clear sky), includes the  $\sim 8000$  cases for which  $r_{es}$  is between 0.85 and 1.05, which is within the uncertainty of the clear-sky model when used as described in section 2.3.

[34] The transitory regime ( $0.6 < r_{es} < 0.85$ ) is not considered. It corresponds to intermediate situations for which the irradiance on the reference radiometer was stable (by virtue of the test performed to check its stability) but the irradiance at larger horizontal scale was likely inhomogeneous. This is probably corresponding to scattered clouds.

[35] The overall frequency content of the fluctuations within the two subsets is displayed on Figure 6, showing very distinct patterns for the *CLOUD* and the *SUN* data sets. The average spectral density in the *CLOUD* data set is maximal for a period of 2.6 seconds (dotted line in Figure 6), and sharply decreases by more than one order of magnitude for smaller periods, indicating that fast fluctuations do not exist under an overcast sky. For the *SUN* data set, the average spectral density is smoother (solid line in Figure 6), with significant periods from 0.6 to 3 seconds, and a maximum spectral density for a period of 1.04s. These periods for the fluctuations in both the *CLOUD* and *SUN* data sets are shorter than the average wave period (between 3 and 6s).

[36] The influence of the other environmental parameters on CV and  $T_{max}$  is now separately examined for the two data

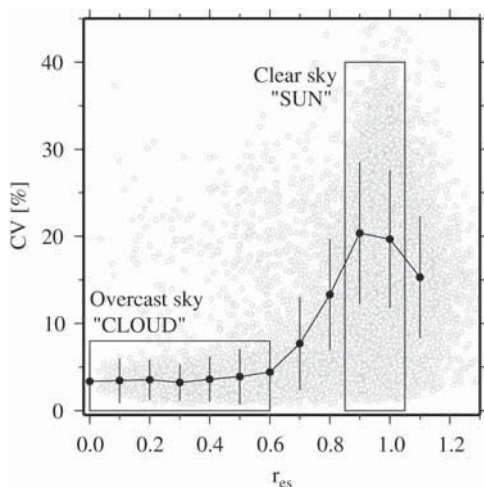


**Figure 5.** Coefficient of variation (CV) for  $E_d(z_u)$  at 510 nm versus  $r_{es}$ . The gray symbols show the complete data set. Solid symbols are the average median and standard deviation for twelve equidistant  $r_{es}$  classes (clusters). The rectangles indicate the boundaries of the *SUN* and *CLOUD* subsets (see text).

sets. For each environmental parameter, each data set has been clustered into equidistant classes. For every class, the average CV and  $T_{max}$ , as well as their respective standard deviation (SD), have been computed. A consequence of rearranging the full data set as a function of different indexes (parameters) is to get different extrema of CV or  $T_{max}$ .

### 3.4. Influence of Environmental Changes on $E_d(z_u, 510)$ Fluctuations Within the *CLOUD* Subset

[37] The changes of CV and  $T_{max}$  within the *CLOUD* data set are displayed as a function of  $\theta_s$  (Figure 7a), wave height (Figure 7b), wind speed (Figure 7c) and  $K_d(490)$  (Figure 7d). In Figure 7, each symbol and the associated vertical bar show the average value and standard deviation of CV or  $T_{max}$  computed over a small range of the environmental parameter in question (e.g.,  $\theta_s$ ), and for the full range of all other environmental parameters (so: wave height, wind speed,  $K_d$ ), except when otherwise stated.

[38] As expected under an overcast sky (vanishing direct radiation), CV is low (steadily around 3%) and nearly independent of the sun altitude (Figure 7a) or the water clarity (Figure 7d). The characteristics of the observed fluctuations depend mostly on the state of the air-sea interface, with CV and  $T_{max}$  regularly and slightly increasing with the wave height (Figure 7b), and, to a lesser extent, with the wind speed (Figure 7c). The average  $T_{max}$  is of about 2.5s, which is half the dominant wave period on the BOUSSOLE site (Figure 4b). It is slightly dependent on the wave height.

### 3.5. Influence of Environmental Changes on $E_d(z_u, 510)$ Fluctuations Within the *SUN* Subset

[39] The changes of CV and  $T_{max}$  within the *SUN* data set are displayed as a function of  $\theta_s$  (Figure 8a), wave height (Figure 8b), the square root of the wind speed (Figure 8c) and  $K_d(490)$  (Figure 8d). In a clear sky, the proportion of diffuse radiation increases as the sun elevation decreases.

This change of the incoming radiation has a strong impact on CV (Figure 8a), which is maximal at 25% when the sun is at its maximum elevation (20% of diffuse radiation; upper scale of Figure 8a), and decreases down to 5% when the sun approaches the horizon (80% of diffuse radiation). This decrease of CV when  $\theta_s$  varies from  $20^\circ$  to  $85^\circ$  is accompanied by an increase of  $T_{max}$  from 1s to 3s. This is due to the progressive decline in direct solar radiation which is responsible for the fastest changes.

[40] The wave height has relatively little influence on CV and  $T_{max}$  (Figure 8b), indicating that the irradiance fluctuations at  $z_u$  are essentially due to capillary waves, whereas gravity waves (i.e., the one measured by the meteorological buoy) have no palpable impact at this depth (the answer might be different at greater depths).

[41] Because the fluctuations we observe here are essentially due to capillary waves, CV and  $T_{max}$  have been plotted as a function of the square root of the wind speed (Figure 8c), which is the parameter that enters into parameterizations of the probability density of surface slopes of capillary waves (e.g., the formalism by *Cox and Munk* [1954]). The coefficient of variation reaches a maximum of about 22% when the wind speed is around  $3 \text{ m s}^{-1}$ , and its overall change with the square root of wind speed has a Gaussian shape, with a slight dissymmetry. Therefore it can be expressed as a combination of a linear function and a Gaussian peak, following:

$$\frac{CV}{CV(0)} = a + b\sqrt{w} + \frac{1}{\sigma\sqrt{2\pi}} e^{-\frac{(\sqrt{w}-c)^2}{2\sigma^2}} \quad (8)$$

where  $CV(0)$  is CV for no wind,  $w$  is wind speed, and  $a = 0.894$ ,  $b = -0.014$ ,  $c = 1.627$  and  $\sigma = 0.752$ . This equation, which is valid in the wind speed range  $[0-16 \text{ m s}^{-1}]$ , provides a generalization for the relative change of CV with wind speed, whereas the particular value of CV for no wind ( $\sim 16\%$  here) might be specific of the measurement conditions of the present work.

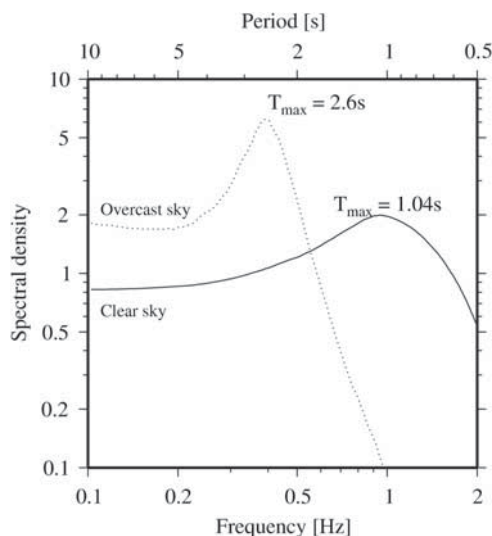


**Figure 6.** Average spectral densities of  $E_d(z_u)$  at 510 nm for the *CLOUD* and *SUN* subsets, as indicated.

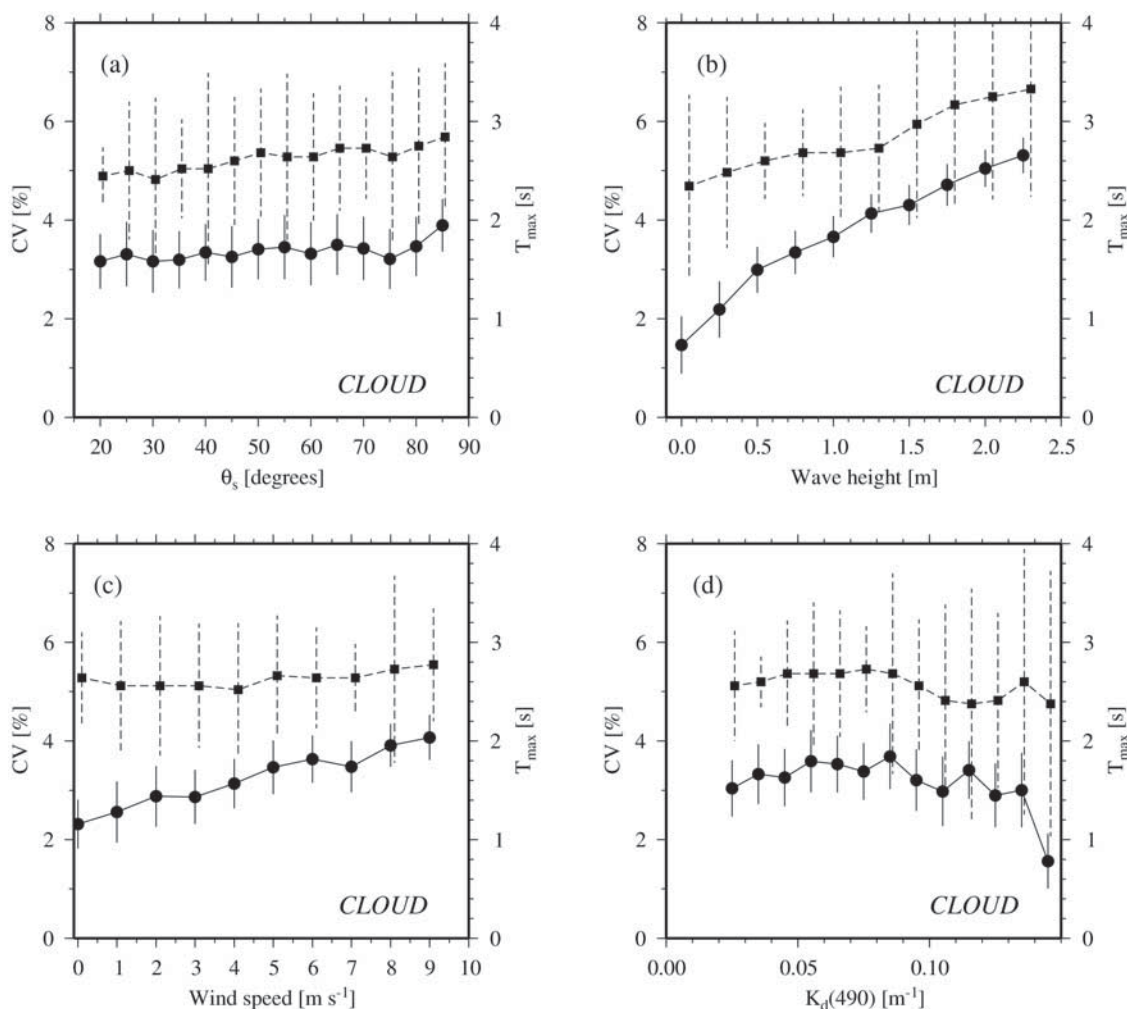


**Figure 7.** Coefficient of variation, CV (solid circles), and period  $T_{\max}$  (solid squares) for  $E_d(z_u)$  at 510 nm within the *CLOUD* subset, as a function of (a)  $\theta_s$ , (b) wave height, (c) wind speed, and (d)  $K_d(490)$ . The symbols are the median values, and the vertical bars are the standard deviations. Note that the  $T_{\max}$  curve is shifted to avoid that error bars for CV and  $T_{\max}$  are superimposed.

[42] The  $T_{\max}$  period varies inversely to CV (Figure 8c). It is minimal at 1.2s for wind speeds between 2 and 4  $\text{m s}^{-1}$  and reaches a maximum of 1.6s as the wind speed increases up to 8  $\text{m s}^{-1}$ .

[43] The other parameter that drives CV is the water clarity (Figure 8d), with CV decreasing from 30% to 12% when  $K_d(490)$  varies from  $\sim 0.03$  to  $\sim 0.15 \text{ m}^{-1}$ . On the contrary, the dominant period of the fluctuations,  $T_{\max}$ , is very little sensitive to changes in  $K_d(490)$ . When the latter increases from 0.02 to 0.07  $\text{m}^{-1}$ , there is only a small increase in  $T_{\max}$  from 1 to 1.5s, and then  $T_{\max}$  remains stable for larger values of  $K_d(490)$ . The standard deviation is large for all classes, which is also an indication that  $K_d(490)$  has little influence on the period of the fluctuations as compared to the other environmental parameters.

[44] Because it was shown (Figure 8a) that the sun zenith angle has a large influence on CV and  $T_{\max}$ , it might be that the examination of their dependence on the other environmental parameters (Figures 8b–8d) is obscured by this strong dependence. The analysis has been, therefore, redone for a subset where  $\theta_s < 40^\circ$ , i.e., a range where the

dependence of CV and  $T_{\max}$  on  $\theta_s$  is small. The dependence of CV on environmental parameters shown in Figures 8b–8d is not appreciably modified (results not shown). The period  $T_{\max}$  no longer shows any change with these parameters.

### 3.6. Depth Changes of $E_d(510)$ Fluctuations

[45] All results have been presented up to now for the upper measurement depth,  $z_u$ , which is around 4 m. Essential differences are now shown when the fluctuations are quantified five meters deeper, at  $z_l$ . The first observation is that variations of CV and  $T_{\max}$  with environmental parameters (such as those displayed in Figure 8) are very similar at  $z_l$  to what they are at  $z_u$  (data not shown).

[46] In order to generalize the observations taken here at two fixed depths, CV and  $T_{\max}$  are plotted as a function of optical depth (OD), i.e., the product  $K_d z$ . The coefficient of variation decreases from about 25% to 15% when OD increases from 0.2 to 0.5 (Figure 9a). This is consistent with the average attenuation of irradiance with depth and with the progressive removal of the largest irradiance peaks

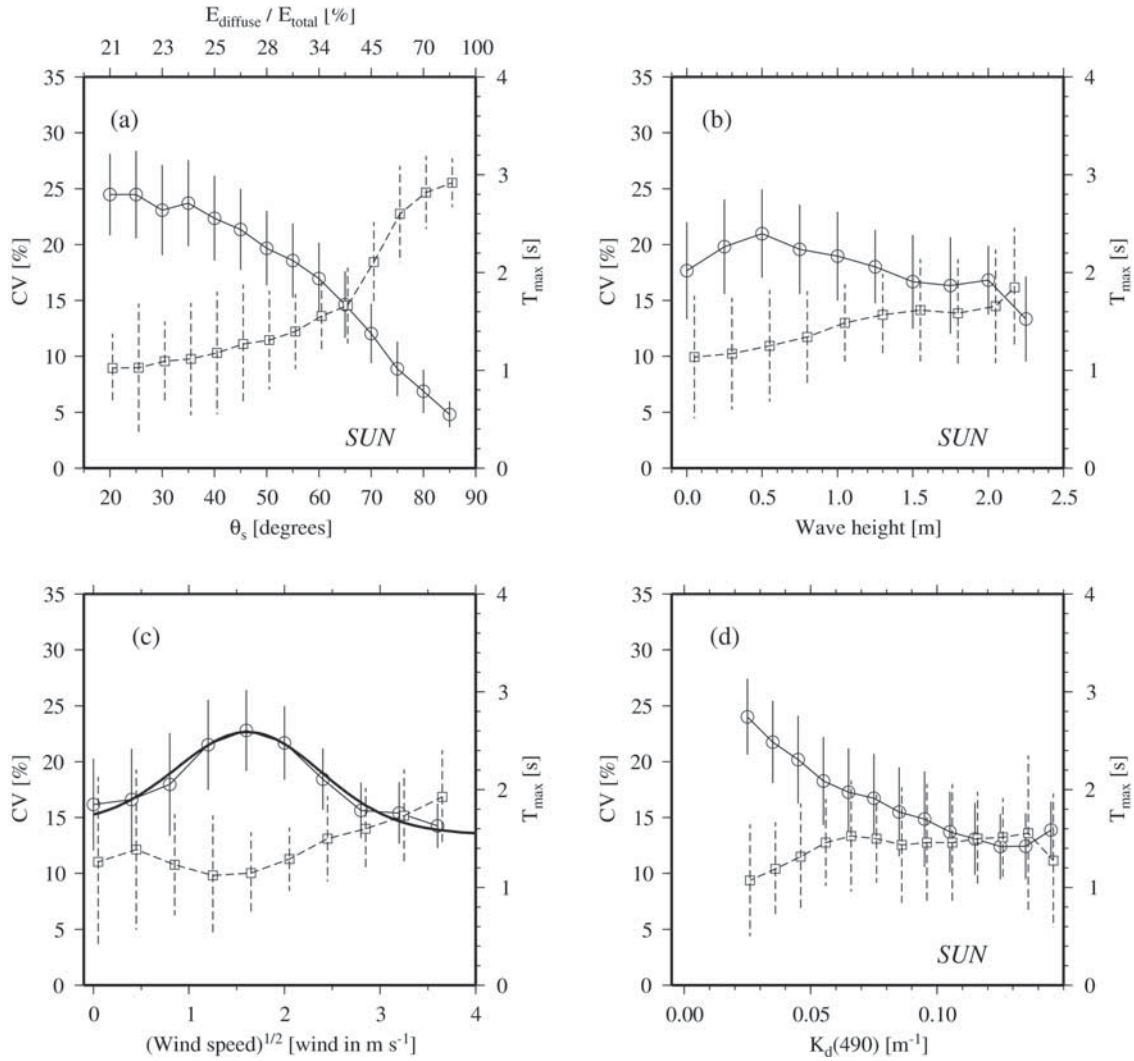


**Figure 8.** As in Figure 7, but for the *SUN* subset, and with the square root of the wind speed used for Figure 8c instead of the wind speed itself. The thick curve on Figure 8c corresponds to equation (8). The ratio of direct to total radiation within the above water downward irradiance [Gregg and Carder, 1990] is indicated on top Figure 8a.

by absorption. The maximum frequency goes from 0.85 Hz to 0.6 Hz over the same optical depth interval (Figure 9b), which is consistent with the observation that the fast fluctuations due to capillary waves (small scale surface roughness) are concentrated near the surface.

[47] In order to complement the results obtained at the two buoy measurement depths, the amplitude of the fluctuations has been also investigated from the vertical  $E_d$  profiles collected with the free-falling instrument deployed during the monthly BOUSSOLE cruises. With such a technique, there is not enough data to determine CV within small depth intervals. Therefore the amplitude is characterized in a different way than for the fixed-depth buoy measurements. A second-order fit is adjusted to the  $E_d$  profiles, and is called  $E_d^*$ , and the relative amplitude of the fluctuations,  $\Delta E_d(z)$ , is computed at the center of 1-m depth bins as:

$$\Delta E_d(z) = \frac{\{\text{Max}(E_d(z_i)) - \text{Min}(E_d(z_i))\}_{z_i \in [z-0.5, z+0.5]}}{E_d^*(z)}, \quad (9)$$

Note that  $\Delta E_d$ , which is based on an absolute difference, is greater than CV, which is based on a standard deviation. The results are also expressed as a function of optical depth (Figure 9a). The amplitude  $\Delta E_d$  is maximal near the surface (average of 40% and values up to 65%), before exponentially decreasing with OD. Fluctuations still exist at two optical depths, with amplitude between 5% and 10%.

### 3.7. Wavelength Dependence of $E_d(z_u)$ Fluctuations

[48] All results have been presented up to now for  $\lambda = 510$  nm, and the spectral changes of CV and  $T_{\max}$  are now examined at the other wavelengths for which irradiance has been recorded (from 442 to 683 nm). The same representation than used in Figure 8 for  $\lambda = 510$  nm is used on Figure 10 for all bands (clear-sky data).

[49] When moving into the electromagnetic spectrum, the shape of the CV curves is essentially preserved, whereas the amplitude changes, with larger CVs for longer wavelengths. An exception occurs when looking at the change of CV with the wave height (Figure 10b), with the shape of the curve being also modified when moving to the red bands. The

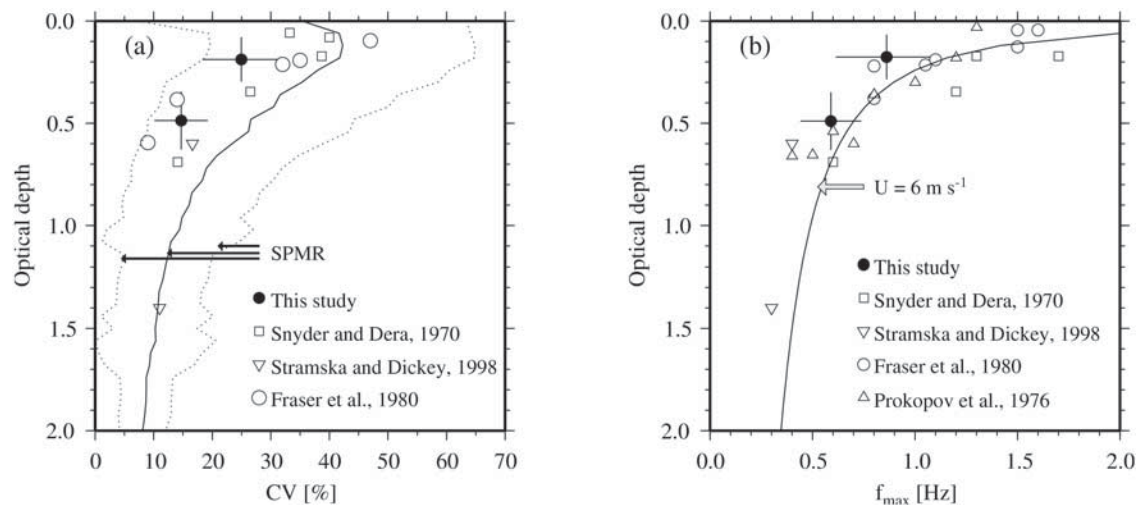


**Figure 9.** (a) Coefficient of variation (CV) as a function of optical depth ( $K_d,z$ ), along with results from previous works (all for  $E_d(525)$ ; open symbols, references as indicated). Solid circles and horizontal lines are, respectively, the median and standard deviation for  $E_d(510)$  at the two buoy measurement depths. Vertical bar indicates the range of optical depth at each of these two depths. Average and extremes of the amplitude of irradiance fluctuations computed from the  $E_d$  profiles (equation (9)) are shown as a continuous and two dotted curves, respectively. (b)  $f_{max}$  as a function of optical depth. The continuous curve corresponds to the theoretical relationship of [Fraser *et al.*, 1980] for a wind speed of  $6 \text{ m s}^{-1}$ .

second obvious change is for the period of the fluctuations, which behave differently in the red and the blue-green domains. Whatever the parameter in question (i.e., Figure 10), the period is identical for all wavelengths up to a certain threshold, after which the period sharply increases in the red whereas it remains constant or slightly increases for other wavelengths.

[50] When all data are pooled together (Figure 11), the average value of CV for clear skies steadily increases from the blue ( $\sim 15\%$ ) to the red ( $\sim 25\%$ ), whereas it is slightly larger only for the red bands in the case of overcast skies. The average  $T_{max}$  period is spectrally flat for clear skies (Figure 11b; standard deviation is much larger in the red, however), whereas two distinct regimes appear under overcast skies, with larger values ( $T_{max} = 6\text{s}$ ) for the red bands. This change is actually due to the effect of waves. When they exceed 1 m,  $T_{max}$  for  $E_d$  fluctuations jumps in the red from 1s to 6s (orange and red curves in Figure 10b). Moreover, CV at these bands increases with wave height, contrary to what is observed at 510 nm and at other wavelengths  $< 600 \text{ nm}$  (blue and green curves in Figure 10).

### 3.8. Fluctuations of the Upward Irradiance

[51] The overall frequency content of the fluctuations for the upward irradiance,  $E_u$ , is displayed on Figure 12 for the two subsets. The patterns are distinct for the *CLOUD* and the *SUN* data sets, but the difference is less pronounced than for  $E_d$  (Figure 6). The average spectral density in the *CLOUD* data set is maximal for long periods ( $T > 5\text{s}$ ; dotted line in Figure 12), and sharply decreases for smaller periods. For the *SUN* data set, the spectral density is equally distributed for periods  $> \sim 3\text{s}$  (solid line in Figure 12). These values are within the range of the average wave period at the BOUSSOLE site (between 3 and 6s).

[52] The changes of CV and  $T_{max}$  for the upward irradiance at 510 nm within the *SUN* data set are displayed as a

function of  $\theta_s$  (Figure 13a), wave height (Figure 13b), wind speed (Figure 13c) and  $K_d(490)$  (Figure 13d). As expected, the fluctuations of  $E_u$  are much fainter than those of  $E_d$  ( $CV \sim 4\%$ ) and their frequency is lower (average  $\sim 4\text{s}$ ). Five meters deeper (at  $z_1$ ), CV is as low as 2% and  $T_{max}$  is around 6 seconds. The approximately opposite changes of CV and  $T_{max}$  for  $E_d$  (Figure 8) are not observed for  $E_u$ , however. On the contrary, both quantities evolve in the same direction when environmental conditions vary. For instance, as  $\theta_s$  increases, CV increases from 1 to 3% and  $T_{max}$  goes from 3.5 to 4.5s (Figure 13a). Larger changes are observed when plotting CV and  $T_{max}$  as a function of the wave height (Figure 13b). Wind speed has little impact on CV and  $T_{max}$  (Figure 13c). Both parameters increase when the water gets less clear (Figure 13d). The impact of cloudiness on CV is very low for the upward irradiance (data not shown).

[53] The spectral changes of the upward irradiance fluctuations are also different than those for the downward irradiance. The coefficient of variation is almost spectrally flat and equal to about 2% for  $\lambda < 600 \text{ nm}$ , and then increases to about 6% in the red (Figure 14a). The average  $T_{max}$  is constant for  $\lambda < 600 \text{ nm}$  under clear skies (dotted line in Figure 14b), whereas it monotonously decreases from 5s (at 442 nm) to 2s (red bands) under overcast skies (solid curve in Figure 14b).

## 4. Discussion and Conclusion

[54] The present work has allowed a characterization of underwater light field fluctuations over an extended range of environmental conditions. The behavior of the amplitude and period of the  $E_d$  fluctuations is generally coherent with previous findings, although a more global picture is provided here.

[55] The most favorable conditions for focusing under clear skies are for wave heights of  $\sim 0.5 \text{ m}$  (Figure 8b) or for

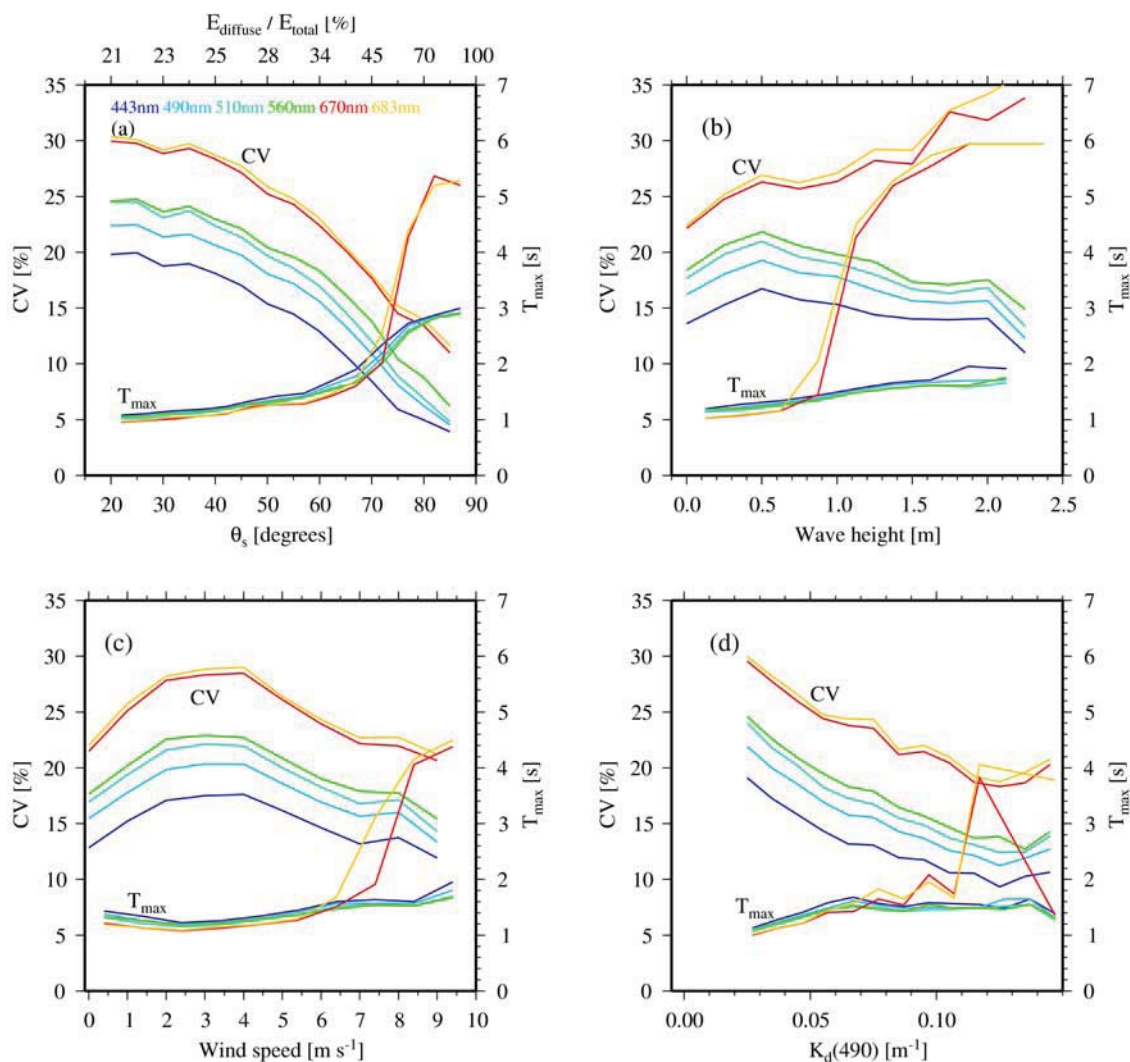


Figure 10. As in Figure 8, but for all bands, as indicated.

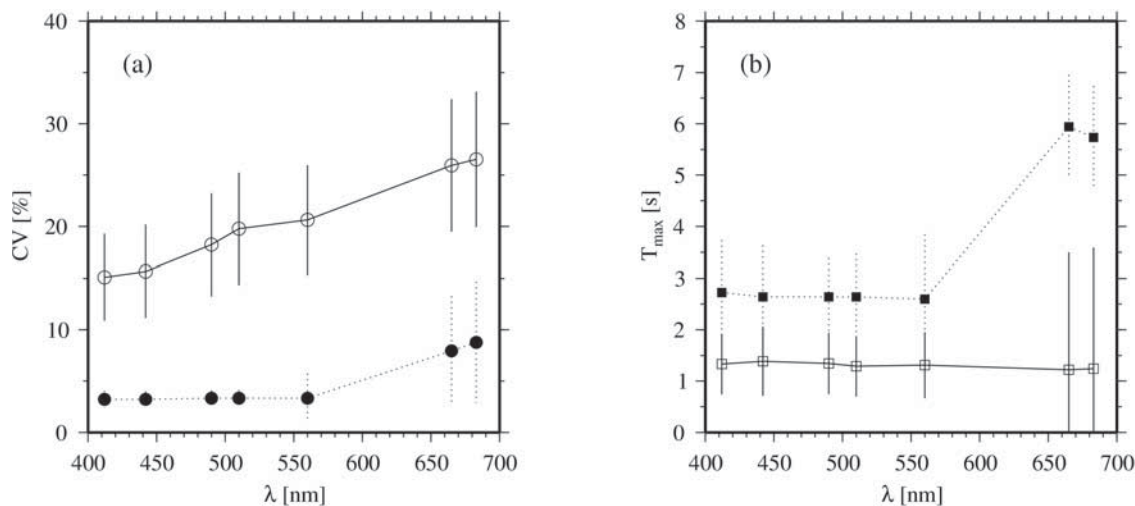
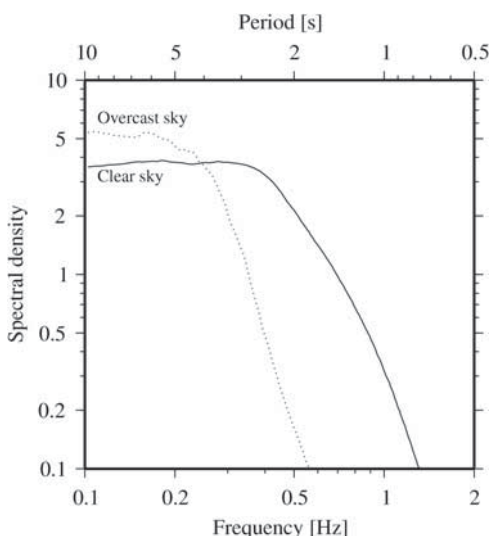


Figure 11. (a) Average coefficient of variation (CV) and (b) average  $T_{max}$  as a function of wavelength, for  $E_d(z_u)$ . Open symbols are for the SUN subset, and solid symbols are for the CLOUD subset.



**Figure 12.** Average spectral densities of  $E_u(z_u)$  at 510 nm for the *CLOUD* and *SUN* subsets, as indicated.

wind speeds between  $\sim 1$  and  $5 \text{ m s}^{-1}$  (Figure 8c). The most unfavorable conditions are for wave heights  $> \sim 1.5 \text{ m}$  or for wind speed  $> 7 \text{ m s}^{-1}$ . The same shape for the same range of wind speed has been previously observed when analyzing the frequency of the brightest flashes [Stramski, 1986]. This confirms that the focusing is intrinsically constituted by a sum of individual fluctuations of different intensities and durations, from milliseconds to a few seconds [Stramski, 1986]. The depth changes of the fluctuations' characteristics reported here (Figure 9) are consistent with the results of previous studies [Fraser et al., 1980; Prokopov and Nikolayev, 1976; Snyder and Dera, 1970; Stramska and Dickey, 1998], which established that the frequency of the fluctuations decreases inversely to the square root of the depth [Fraser et al., 1980].

[56] Regarding the spectral changes, the abrupt change of  $T_{\max}$  in the red when the wave height exceeds 1 m (Figures 10 and 11) suggests that two phenomena alternatively determine the period of irradiance fluctuations. The short periods are attributable to the focusing by capillary waves, whereas the slower regime can be attributed to fluctuations in optical depth associated with the passage of swells. The value of 6s for  $T_{\max}$  is coherent with an average wave period of 6.3s, as recorded for waves higher than 2 m

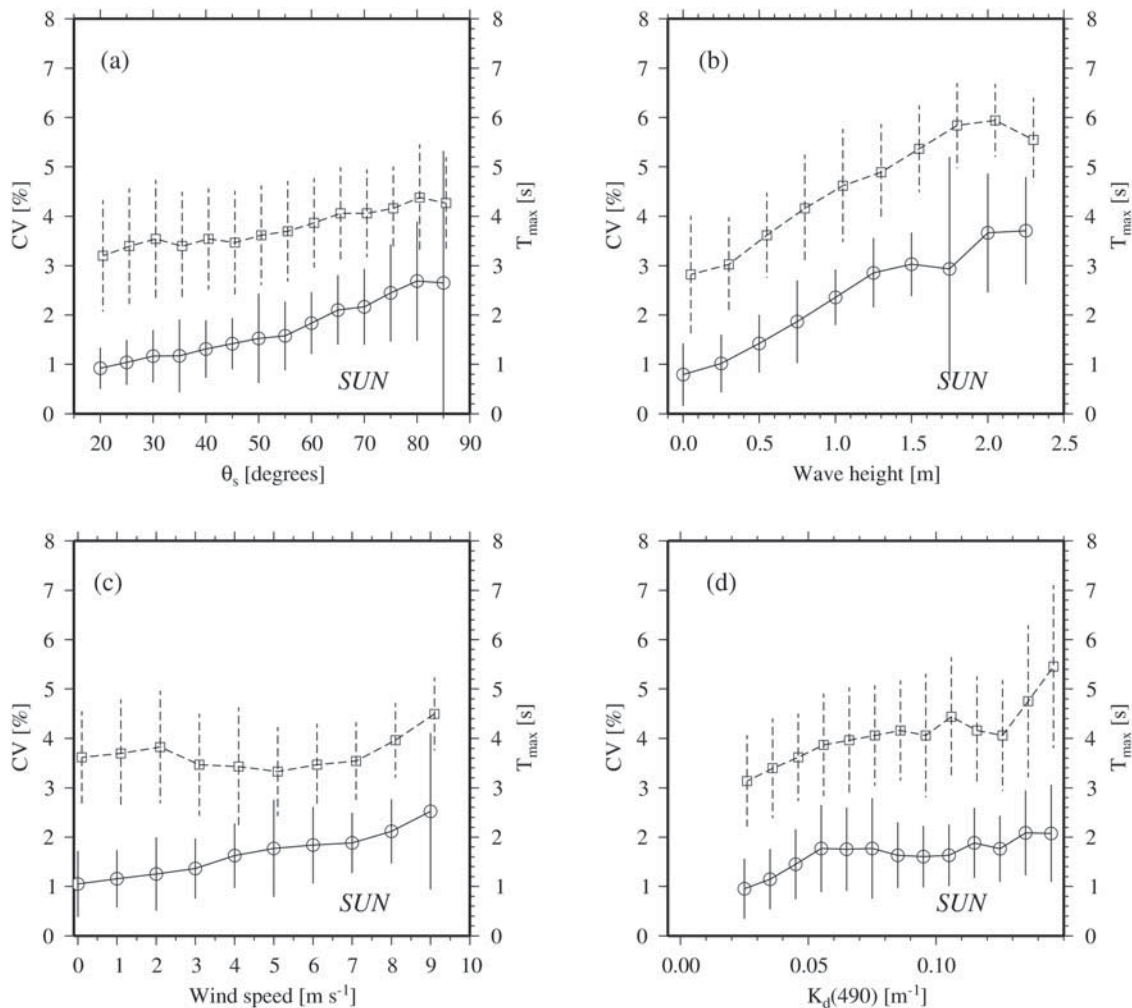


**Figure 13.** As in Figure 8, but for  $E_u(z_u)$  at 510 nm within the *SUN* subset.

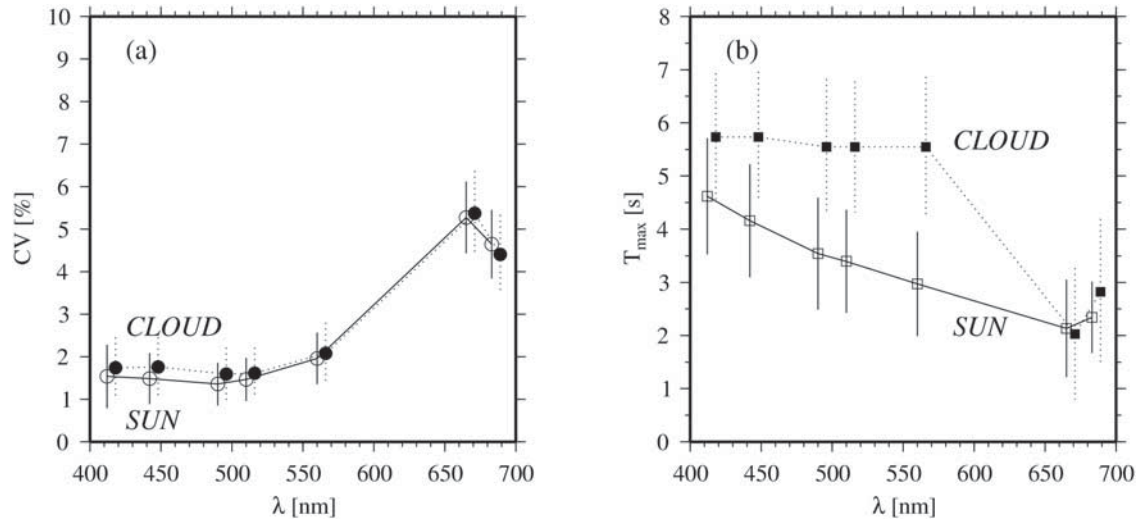


**Figure 14.** (a) Coefficient of variation (CV) and (b)  $T_{\max}$  as a function of wavelength, for  $E_u(z_1)$ . Open symbols are for the SUN subset, and solid symbols are for the CLOUD subset.

at BOUSSOLE. When a wave of height  $h$  passes over the mooring, the thickness of the water column above the sensor varies between  $z - h/2$  and  $z + h/2$ . The resulting relative change in irradiance,  $\Delta E_d(\lambda, z)$ , depends on  $h$  and  $K_d$ :

$$\begin{aligned} \Delta E_d(\lambda, z) &= \frac{E_d(\lambda, z + h/2) - E_d(\lambda, z)}{E_d(\lambda, z)} \\ \Delta E_d(\lambda, z) &= \frac{E_d(\lambda, z) \exp[(h/2) K_d(\lambda)] - E_d(\lambda, z)}{E_d(\lambda, z)} \\ \Delta E_d(\lambda, z) &= \exp[(h/2) K_d(\lambda)] - 1 \end{aligned} \quad (10)$$

To illustrate equation (10),  $\Delta E_d(\lambda, z)$  was computed with  $K_d(\lambda)$  derived from [Morel and Maritorena, 2001], assuming a chlorophyll concentration of  $0.1 \text{ mg}\cdot\text{m}^{-3}$ , and with  $h$  between 0.2 and 2 m (Figure 15). These changes have very little influence in the blue and green part of the electromagnetic spectrum, whereas they generate changes in  $E_d$  of at least 40% in the red, as soon as the wave height exceeds 1 m.

[57] The diffuse attenuation of  $E_d$  results from a combination of absorption,  $a$ , and backscattering,  $b_b$  [Gordon, 1989; Morel and Gentili, 2004], so it is worth examining separately the influence of  $a$  and  $b_b$  on CV and  $T_{\max}$ . This is shown here for  $\lambda = 510 \text{ nm}$  (Figure 16), using values of  $a$  and  $b_b$  derived from  $K_d$  and  $R$  through the inversion procedure proposed by Morel *et al.* [2006]. As far as absorption is concerned, the dimensionless product  $a \cdot z$  is used here, in order to generalize our results in terms of optical depth.

[58] The fastest and brightest components of the fluctuations, which focus at the shallowest depths, are expected to be removed as the absorption increases. This is indeed observed here, with a decrease of CV at  $z_1$  from 30 to 5% when the absorption optical depth varies from 0 to 0.35 (Figure 16a). At the same time,  $T_{\max}$  increases from 1 to

3 seconds. Overall, CV follows an inverse dependency to optical depth, which can be expressed as:

$$\frac{CV(a \cdot z)}{CV(0)} = 1 - 2.376 a \cdot z \quad (11)$$

[59] No significant effect of backscattering is observed on CV and  $T_{\max}$  (Figure 16b). This observation might become invalid for a larger range of the backscattering coefficient (coastal waters for instance).

[60] It is usually assumed that the characteristics of the fluctuations for the upward flux are similar to those of the downward flux, except for their amplitude. The analysis performed here provides some counterintuitive results, showing for instance that the amplitude of the  $E_u$  fluctuations (CV) decreases as the water becomes clearer. This goes in the opposite direction as compared to  $E_d$ . As the

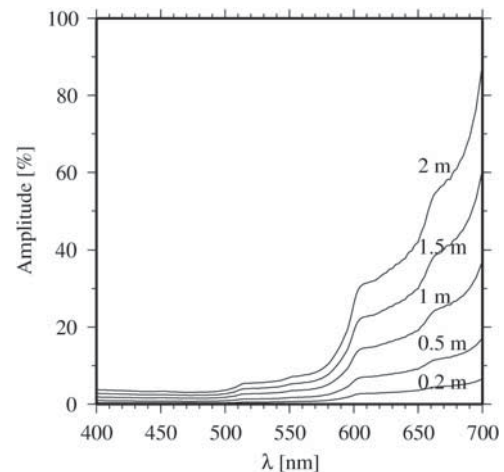


**Figure 15.** Theoretical amplitude of irradiance fluctuations related to variations of optical depth due to waves of various heights (as indicated), as a function of wavelength.

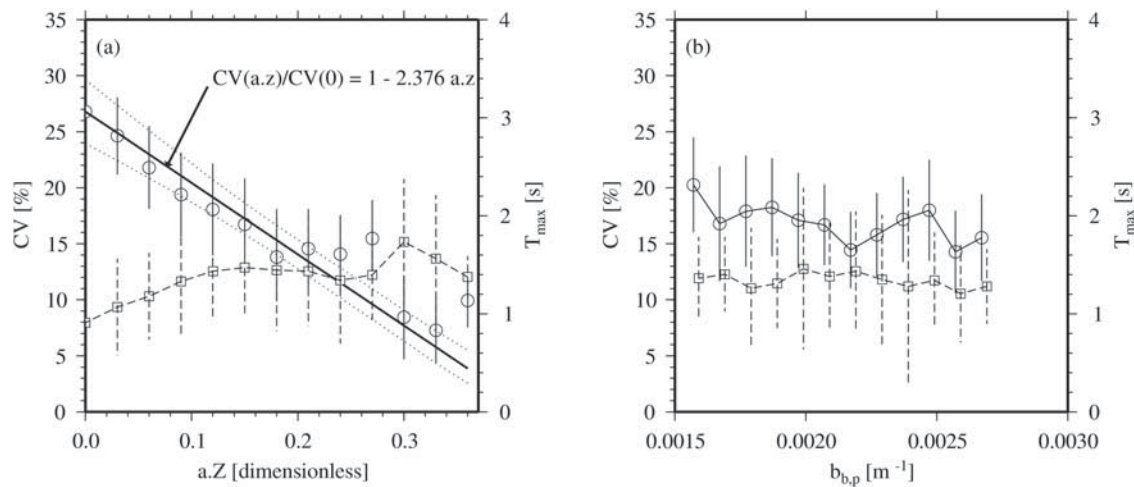


**Figure 16.** Coefficient of variation (CV; circles) and  $T_{max}$  (squares) for  $E_d(z_u)$  at 510 nm, as a function of the absorption optical depth, i.e., (a) the product  $a.z$  and of (b) the backscattering coefficient at 490 nm. Data are from the *SUN* subset. In Figure 16a, the solid curve corresponds to equation (11).

water becomes clearer, the upward flux at a given depth is formed by backscattered photons that have possibly traveled at deeper depths, resulting in more scattering events. The target to which a downward-looking irradiance sensor is aiming at is more and more diffuse as the water body is clearer, which explains the behavior of CV observed here.

[61] Similarly, the other environmental changes have the inverse effect on CV for  $E_u$  than for  $E_d$ . As  $\theta_s$  increases, the increase in the diffuse to total irradiance ratio results in an increase in CV (Figure 13a). The variations in  $T_{max}$  are easier to interpret. For the fluctuations in the upward flux,  $T_{max}$  increases in response to the increase in  $T_{max}$  for the downward flux.

[62] Besides the thorough characterization of the underwater light field fluctuations that was feasible here thanks to

the analysis of a long time series, next steps are to perform similar analyses on data collected at higher frequencies in order to better sample very bright and short flashes. Another important research area will be to understand the relationships between the fluctuations' characteristics and the three-dimensional properties of the air-sea interface.

**Appendix A: Determining the Frequency Content of the Fluctuations**

[63] In order to characterize the frequency content of the fluctuations, the spectral density of the recorded signal is computed. The usual way of doing this is to use a Fast Fourier Transform (FFT). The buoy's acquisition sequences only include about 360 measurements, however, which is an

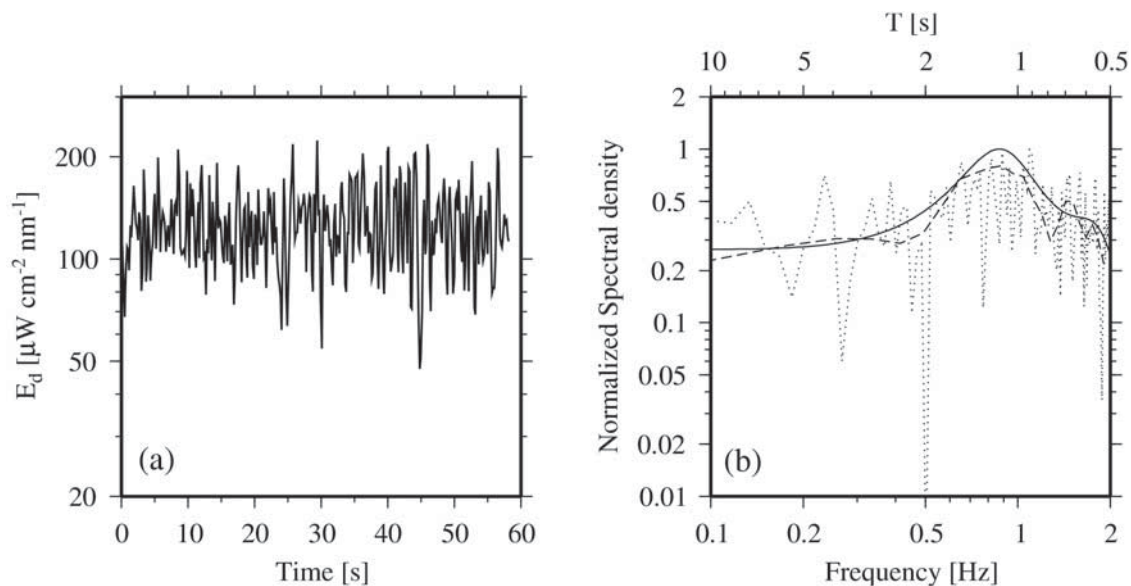


**Figure A1.** (a) Measurement sequence for  $E_d(z_u)$  at 510 nm, performed on 1 August 2007 at 1200 UTC and under a clear sky (same data as in Figure 3a). (b) Normalized Spectral Densities of the signal shown in Figure A1a, obtained using three methods: module of the Fast Fourier Transform (FFT, dotted curve), Blackman-Tukey method (BT, dashed curve), and Auto Regressive Model (AR, solid curve).

insufficient number of points to safely compute the spectral density using a FFT (a minimum of 512 points is recommended). The autoregressive model (AR) is better adapted in such conditions [Legendre and Legendre, 1998]. This is a predictive model, where the spectral density is estimated by a set of autoregressive coefficients  $\phi_k$ . These coefficients are determined using the data series itself, that is, the signal measured at time  $t$  is represented as a function of the  $q$  preceding observations:

$$y_t = \phi_1 y_{t-1} + \phi_2 y_{t-2} + \dots + \phi_q y_{t-q} + a_t,$$

where  $a_t$  is a residual value,  $\phi_k$  are the autoregressive coefficients and  $q$  is the order of the model: it specifies how many steps back one takes into account to predict the value  $y_t$ . The function spectrum [R Development Core Team, 2008; Venables and Ripley, 2002] has been used to determine the coefficients and the order of the autoregressive model.

[64] To illustrate the skill of the AR model, a typical clear-sky time series (Figure A1(a)) has been processed with the AR model, a Fast Fourier Transform, and also the conventional Blackman-Tukey (BT) method [Bendat and Piersol, 1966], which was also used by Stramska and Dickey [1998] to characterize spectral density of light fluctuations. The three spectrograms are displayed in Figure A1(b). As expected, the use of the module of a Fast Fourier Transform (FFT) is not optimal. The AR and BT methods give equivalent results.

[65] **Acknowledgments.** Pierre Gernez benefited from a grant provided by the ACRI-st company and the French National Association for Research and Technology (ANRT). The BOUSSOLE project is supported and funded by the Centre National de la Recherche Scientifique (CNRS), the Institut National des Sciences de l'Univers (INSU), the French space agency "Centre National d'Etudes Spatiales" (CNES), the European Space Agency (ESA/ESTEC-ESRIN), and the National Aeronautics and Space Administration of the United States (NASA) through a Letter of Agreement with the Université Pierre et Marie Curie (UPMC, Paris). We are grateful to Tommy Dickey and one anonymous reviewer for their comments and suggestions.

## References

- Antoine, D., et al. (2006), BOUSSOLE: A Joint CNRS-INSU, ESA, CNES and NASA Ocean Color Calibration and Validation Activity, *NASA Tech. Memo., TM-2006-214147*, 59 pp., NASA GSFC, Greenbelt, Md.
- Antoine, D., P. Guevel, J.-F. Desté, G. Bécu, F. Louis, A. Scott, and J. Bardey (2008a), The "BOUSSOLE" buoy. A new transparent-to-swell taut mooring dedicated to marine optics: Design, tests and performance at sea, *J. Atmos. Oceanic Tech.*, 25, 968–989.
- Antoine, D., F. d'Ortenzio, S. B. Hooker, G. Bécu, B. Gentili, D. Tailliez, and A. J. Scott (2008b), Assessment of uncertainty in the ocean reflectance determined by three satellite ocean color sensors (MERIS, SeaWiFS and MODIS-A) at an offshore site in the Mediterranean Sea (BOUSSOLE project), *J. Geophys. Res.*, 113, C07013, doi:10.1029/2007JC004472.
- Austin, R. W. (1974), The remote sensing of spectral radiance from below the ocean surface, in *Optical Aspects of Oceanography*, edited by N. G. Jerlov and E. Steemann-Nielsen, pp. 317–344, Elsevier, London, U. K.
- Bendat, J. S., and A. G. Piersol (1966), *Measurements and Analysis of Random Data*, 390 pp., Wiley, New York.
- Cox, C., and W. Munk (1954), Statistics of the sea surface derived from sun glitter, *J. Mar. Res.*, 13, 198–227.
- Dera, J. (1970), On two layers of different light conditions in the euphotic zone of the sea, *Acta Geophys. Pol.*, 18, 287–294.
- Dera, J., and H. R. Gordon (1968), Light field fluctuations in the photic zone, *Limnol. Oceanogr.*, 13, 697–699.
- Dera, J., S. Sagan, and D. Stramski (1993), Focusing of sunlight by sea surface waves: New results from the Black Sea, *Oceanologia*, 34, 13–25.
- Fraser, A. B., R. E. Walker, and F. C. Jurgens (1980), Spatial and temporal correlation of underwater sunlight fluctuations in the sea, *IEEE J. Oceanic Eng.*, 5, 195–198.
- Frechette, M., and L. Legendre (1978), Phytoplankton photosynthesis: Response to a simplified stimulus modelling rapid light fluctuations induced by sea surface waves, *J. Exp. Mar. Biol. Ecol.*, 32, 15–25.
- Gordon, H. R. (1989), Can the Lambert-Beer law be applied to the diffuse coefficient of ocean water?, *Limnol. Oceanogr.*, 34, 1389.
- Gregg, W. W., and K. L. Carder (1990), A simple spectral solar irradiance model for cloudless maritime atmospheres, *Limnol. Oceanogr.*, 35, 1657–1675.
- Legendre, P., and L. Legendre (1998), *Numerical Ecology*, 2nd English ed., xv + 853 pp., Elsevier Sci., Amsterdam.
- Legendre, L., M. Rochet, and S. Demers (1986), Sea-ice microalgae to test the hypothesis of photosynthetic adaptation to high frequency light fluctuations, *J. Exp. Mar. Biol. Ecol.*, 97, 321–326.
- McFarland, W., and E. Loew (1983), Wave produced changes in underwater light and their relations to vision, *Environ. Biol. Fishes*, 8, 173–184.
- Millot, C. (1999), Circulation in the Western Mediterranean sea, *J. Mar. Syst.*, 20, 423–442.
- Morel, A., and B. Gentili (2004), Radiation transport within oceanic (case 1) water, *J. Geophys. Res.*, 109, C06008, doi:10.1029/2003JC002259.
- Morel, A., and L. Prieur (1977), Analysis of variations in ocean color, *Limnol. Oceanogr.*, 22, 709–722.
- Morel, A., and S. Maritorena (2001), Bio-optical properties of oceanic waters: A reappraisal, *J. Geophys. Res.*, 106(C4), 7163–7180.
- Morel, A., B. Gentili, M. Chami, and J. Ras (2006), Bio-optical properties of high chlorophyll Case 1 waters and of yellow-substance-dominated Case 2 waters, *Deep Sea Res. I*, 53, 1439–1459.
- Prokopov, O. I., and V. P. Nikolayev (1976), A study of the underwater illumination fluctuations in the Mediterranean Sea, *Izv. Oceanic Phys.*, 12, 340–342.
- Queguiner, B., and L. Legendre (1986), Phytoplankton photosynthetic adaptation to high-frequency light fluctuations simulating those induced by sea-surface waves, *Mar. Biol.*, 90, 483–491.
- R Development Core Team (2008), R Found. for Stat. Comput., Vienna, Austria. (Available at <http://www.R-project.org>)
- Rosow, W. B., and R. A. Schiffer (1991), ISCCP cloud data products, *Bull. Am. Meteorol. Soc.*, 72, 2–20.
- Schenck, H. (1957), On the focusing of sunlight by ocean waves, *J. Opt. Soc. Am.*, 47, 653–657.
- Schippnick, P. F. (1988), Imaging of a bottom object through a wavy air-water-interface, *SPIE Proc.*, 925, 371–382.
- Shettle, E. P., and R. W. Fenn (1979), Models for the aerosols of the lower atmosphere and the effects of humidity variations on their optical properties, *Environmental Research Papers*, 676, AFGL-TR-79-0214, Air Force Geophys. Lab., AFB, Mass., 20 Sept.
- Snyder, R. L., and J. Dera (1970), Wave-induced light-field fluctuations in the sea, *J. Opt. Soc. Am.*, 60, 1072–1079.
- Stramska, M., and T. D. Dickey (1998), Short-term variability of the underwater light field in the oligotrophic ocean in response to surface waves and clouds, *Deep Sea Res. I*, 45, 1393–1410.
- Stramski, D. (1986), Fluctuations of solar irradiance induced by surface waves in the Baltic, *Bull. Pol. Acad. Sci. Earth Sci.*, 34, 333–344.
- Stramski, D., G. Rosenberg, and L. Legendre (1993), Photosynthetic and optical properties of the marine chlorophyte *Dunaliella tertiolecta* grown under fluctuating light caused by surface-wave focusing, *Mar. Biol.*, 115, 363–372.
- Venables, W. N., and B. D. Ripley (2002), *Modern Applied Statistics With S-PLUS*, 4th ed., Springer, New York.
- Walker, R. E. (1994), *Marine Light Field Statistics*, Wiley, New York.
- Walsh, P., and L. Legendre (1983), Photosynthesis of natural phytoplankton under high frequency light fluctuations simulating those induced by sea surface waves, *Limnol. Oceanogr.*, 28, 688–697.
- Zaneveld, J. R. V., E. Boss, and A. Barnard (2001), Influence of surface waves on measured and modeled irradiance profiles, *Appl. Opt.*, 40, 1442–1449.
- Zibordi, G., D. d'Alimonte, and J. F. Berthon (2004), An evaluation of depth resolution requirements for optical profiling in coastal waters, *J. Atmos. Oceanic Tech.*, 21, 1059–1073.

D. Antoine, UMR 7093, Laboratoire d'Océanographie de Villefranche, CNRS-UPMC Paris 06, Quai de la Darse, BP 8, 06238 Villefranche-sur-mer Cedex, France.

P. Gernez, ACRI-st, 260 route du Pin Montard, BP 234, 06904 Sophia Antipolis Cedex, France. (pgernez@obs-vlfr.fr)